remote sensing

MDPI

Article

Variability in the Sea Surface Temperature Gradient and Its Impacts on Chlorophyll-a Concentration in the Kuroshio Extension

Yuntao Wang *, Rui Tang, Yi Yu and Fei Ji

State Key Laboratory of Satellite Ocean Environment Dynamics, Second Institute of Oceanography, Ministry of Natural Resources, Hangzhou 310012, China; ruitang@sio.org.cn (R.T.); yiyu@sio.org.cn (Y.Y.); jfmy@sio.org.cn (F.J.)

* Correspondence: yuntao.wang@sio.org.cn; Tel.: +86-571-8196-3629

Abstract: Sixteen years of satellite observational data in the Northwestern Pacific Ocean are used to describe the variability in the sea surface temperature (SST) gradient and its impact on chlorophyll-a concentrations (Chl-a). Spatially, a meridional dependence is identified in which the SST gradient increases to the north in association with elevated Chl-a. Temporally, the seasonal variability shows a large SST gradient and high Chl-a in winter and spring, while the SST gradient and Chl-a are much lower in summer. The seasonal variability in Chl-a leads the variability in the SST gradient by one month. A significant correlation between the SST gradient and Chl-a in the anomalous field is obtained only in the western section of the Kuroshio extension (KE) and the highest correlation is identified without any lags. An index for the section is defined as the proportion of the number of times that the SST gradient magnitude is anomalously large in each year, and the index is highly related to the stability of the KE and has a prominent influence on Chl-a in the region. An anomalously large positive (negative) SST gradient magnitude occurs when the KE is unstable (stable) and the corresponding Chl-a is high (low).

Keywords: sea surface temperature gradient; Kuroshio extension; chlorophyll-a; dynamic stability; remote sensing

check for updates

Citation: Wang, Y.; Tang, R.; Yu, Y.; Ji, F. Variability in the Sea Surface Temperature Gradient and Its Impacts on Chlorophyll-a Concentration in the Kuroshio Extension. *Remote Sens.* **2021**, *13*, 888. https://doi.org/10.3390/rs13050888

Academic Editor: Yukiharu Hisaki

Received: 2 January 2021
Accepted: 22 February 2021
Published: 26 February 2021

Publisher's Note: MDPI stays neutral with regard to jurisdictional claims in published maps and institutional affiliations.

Copyright: © 2021 by the authors. Licensee MDPI, Basel, Switzerland. This article is an open access article distributed under the terms and conditions of the Creative Commons Attribution (CC BY) license (https://creativecommons.org/licenses/by/4.0/).

1. Introduction

In the northwestern Pacific Ocean, there are two major currents, the Kuroshio current and the Oyashio current, which flow from the southwest and northeast, respectively [1]. These currents are crucial for the meridional transport of water and heat in the region and play an important role in global circulation [2]. In the subtropical region, water piles up in the western section of the Pacific Ocean, and as the large westward pressure gradient balances with the Coriolis forces, an intense northward current, the Kuroshio current, is generated following the Sverdrup theory [3]. As one of the major western boundary currents in the world, the Kuroshio current is characterized by warm temperatures and high salinities [4]. It can extend more than 1000 m in depth and transport substantial quantities of water, i.e., 42 Sv excluding the local recirculation, and energy into the mid-latitude region [5]. Conversely, the Oyashio current has low temperatures and salinities and is high in nutrients, which can impact the mortality rate of small pelagic fishes [6]. The annually averaged transport of the Oyashio current is 31 Sv, with a larger value during winter [7]. Both currents converge east of Japan, and the confluence flows eastward, where it is subsequently referred to as the Kuroshio extension (KE) [8]. The region of the KE is characterized by a prominent gradient in sea surface height (SSH), with the SSH decreasing from the subtropical gyre toward the north [8]. In particular, intense changes in SSH can be found to the east of Japan where the KE transports a large volume of water masses associated with high quantities of nutrients and CO_2 [9,10]. The eastward transport of

the KE is indeed found to be highly related to the change in SSH across the KE [5]. The energetic KE is characterized by stationary meanders and sheds mesoscale eddies that separate from the meanders [1]. The zonal extent of the KE is usually defined as the region between the coast of Japan and the 165° E meridian, where upstream and downstream of the KE are defined as the regions to the west and east of 153° E, respectively [11]. In particular, the upstream region of the KE is characterized by large seasonal and interannual to decadal variability [12].

Because of the convergence of the two major currents, prominent instability is introduced, and the eddy kinetic energy (EKE) in the region is one of the largest in the world [12]. In particular, mesoscale processes, e.g., fronts and eddies, are abundant in the KE and play an important role in determining regional dynamics and subsequently influencing regional ecosystems. The oceanic fronts delineate the boundaries between water masses, which are characterized by different temperatures, nutrients, and other parameters [13]. The frontal zone in the ocean can be associated with an extremely large concentration of phytoplankton, e.g., diatoms [13]. The sea surface temperature (SST) is a major feature for delineating water masses, and the SST gradient is widely used to detect fronts [14]. SST gradient-derived fronts have been investigated in major current systems, e.g., eastern boundary currents [15], the Gulf Stream [16], and the Brazil current [17]. Fronts in coastal regions can be highly correlated with the local upwelling, which introduces subsurface cold water to the surface and induces fronts [14,15,17]. Similarly, wind can induce mixing and Ekman pumping in the open ocean, leading to cooling at the surface and driving frontogenesis [18]. In return, the difference in SST on each side of a front can modulate the stability of the atmospheric boundary layer and result in increasing (deceasing) wind over warm (cold) surfaces [16]. Thus, the frontal zone is usually characterized as a highly dynamic region that includes the convergence of water masses [18] associated with high nutrients contents and primary production [13,19]. In particular, when the alongshore wind drives coastal upwelling on the coast of California [15], the upwelled cold and nutrient-rich water converges with warm surface water [14]. Fronts are subsequently generated at the boundary of the upwelling zone, which is associated with increased phytoplankton [20]. Similarly, a connection between the front and phytoplankton is also expected in the KE region, which should be further explored.

The biomass of phytoplankton can be gauged by the chlorophyll-a concentrations (Chl-a) [21], which can be measured by remote sensing at a global scale with high spatial resolution, i.e., 1/24° or higher [22]. Long-term satellite observations can detangle the major components of Chl-a variability, e.g., the annual cycle and interannual variations [22]. A prominent seasonal cycle has been identified in which high Chl-a levels occur in local summer when wind-induced frontal activities are enhanced [15]. Because surface fronts can be detected via the SST gradient, a simplified approach has been developed by linking the SST gradient with the Chl-a concentration to identify their dependence [23]. In addition to the investigation of seasonal variability, the underlying dynamics between frontal activities and Chl-a have been further confirmed in an anomalous field, which is obtained by removing the monthly climatology [15]. Wang et al. [23] found that as the wind anomaly increases, there are larger SST gradients (fronts) and higher Chl-a levels because wind mixing cools the SST and brings more nutrients into the euphotic zone. Yu et al. [24] revealed a significant dependence between frontal activities and Chl-a and found that high Chl-a is accompanied by high frontal activities both during seasonal cycles and in an anomalous field.

Eddies, as another class of mesoscale dynamics, are important for driving vertical mixing and horizontal advection. Upwelling (downwelling) occurs in cyclonic (anticyclonic) eddies that can depress (elevate) the ocean surface, and a closed contour of the sea level anomaly (SLA) can be applied to identify the eddy location [25]. Simultaneously, the mixed layer depth (MLD) will be reduced (increased) in cyclonic (anticyclonic) eddies [26]. Thus, eddies induce a monopole feature at their center, and the amplitude of the monopole decreases with the distance from the center of the eddy [27]. If a prominent horizontal

gradient exists in water parameters, e.g., SST and Chl-a, the rotation of eddies can advect water and induce a dipole feature [28]. The intensity of the dipole increases with the strength of the background gradient, although the redistribution of parameters induces no change in total SST or Chl-a [29]. Compared with the dipole pattern, the monopole feature is usually dominant in major global oceans, including the Kuroshio current and KE, Gulf Stream and eastern boundary current systems [25,30]. More nutrient-rich subsurface water is transported into the euphotic layer within cyclonic eddies, leading to high surface Chl-a [26,27,31]. In contrast, the limited nutrients in anticyclonic eddies inhibit the growth of phytoplankton and result in low Chl-a [29]. Thus, a negative relationship can be found between the SLA and Chl-a when mesoscale eddies dominate the dynamics [32]. This phenomenon is particularly true for oligotrophic regions, including the region south of the KE, where the growth of phytoplankton is limited by the availability of nutrients [33]. Different mechanisms for generating eddies are found in the KE than in other boundary currents, including pinching off from the main stream [34] and horizontal shear instability [35]. Longer-lived and larger cyclonic (anticyclonic) eddies are found to the south (north) of 35° N [36]. Because the water masses inside and outside of the eddy perimeters are usually distinct from each other, the boundary of eddies can be identified as fronts if the difference between them is prominent [30,33]. Many studies have investigated the impact of mesoscale eddies on the Chl-a distribution and ecosystem variability in the KE [32,33,37]; however, the influence of eddy-induced frontal activities on Chl-a has been much less studied.

Dynamics are important for driving the regional variability in Chl-a at seasonal scales and in anomalous fields [14,15,29]. Prominent decadal variability in Chl-a has also been identified in the KE [38] and is modulated by large-scale and long-term dynamic processes. The variability of the KE is characterized by two distinct modes: stable and unstable modes [12]. A contour of SSH with a specific value, e.g., 110 cm or 170 cm, can be applied such that a longer (shorter) pathlength of the contour indicates an unstable (a stable) dynamic state [39]. The dynamic processes and associated oceanic parameters show more complex variation when the KE is in the unstable mode and less variation when the KE is in the stable mode [12,39,40]. The dynamic state can be reflected via the SSH anomaly, as the SSH anomaly is positive (negative) during the stable (unstable) mode [39]. The switch between the dynamic states is related to the first Pacific decadal mode, namely, the Pacific decadal oscillation (PDO) [41]. In particular, the positive PDO generates negative SSH anomalies in the eastern Pacific Ocean, which are transported westward via baroclinic Rossby waves [40]. As a Rossby wave propagates westward, it pushes the KE southward, such that the deep KE interacts with the shallow Shatsky Ridge and generates instability, leading to an unstable mode of KE [41]. Conversely, the negative PDO induces positive SSH anomalies that are less favorable for generating instability, and the KE switches to the stable mode. Subsequently, a large (small) instability during the unstable (stable) mode can enhance (depress) eddy activities and subsequently enhance Chl-a variability in the KE [38]. The second Pacific decadal mode, the North Pacific Gyre Oscillation (NPGO) index, can also influence the KE strength and ecosystem variability with a lag of 2 to 4 years [42] because of the time required for the signal to propagate westward [43]. However, the connection between the interannual variability in the stability of the KE and the corresponding SST gradient has not yet been resolved, e.g., the intensity of the SST gradient in response to different modes of KE status and the timing for the response to occur. Additionally, the impact of the interannual variability in the SST gradient on Chl-a should be further explored.

Local dynamics in the KE have a prominent impact on marine primary production and subsequently influence the higher trophic levels, e.g., zooplankton [44,45] and fishery resources [46]. A clear dependence has been identified between the dynamics and the distribution of Chl-a; however, the detailed relationship at seasonal and interannual scales, and in anomalous fields has not been clearly resolved. In particular, whether this dependence is valid over the entire region or limited to a certain spatial extent, and what

the timing of different dynamics impacting Chl-a, are unclear. In this study, long-term satellite observations of the SST gradient and Chl-a are used to identify the region with a significant relationship between these factors at different scales and with the underlying dynamics. The remainder of the paper includes the materials and methods in Section 2, the results in Section 3, the discussion in Section 4 and the conclusions in Section 5.

2. Materials and Methods

Satellite observations of SST and Chl-a are used in this study to represent oceanic conditions. Daily observations measured by the Moderate Resolution Imaging Spectroradiometer (MODIS) onboard NASA's satellite Aqua are obtained with level-3 datasets at a spatial resolution equal to $1/24^{\circ}$, e.g., 4.5 km. The dataset covers a long time period from July 2002 to the present; please refer to the acknowledgements section for detailed information on data availability. The cloud coverage is identified and excluded before distributing the dataset. Remotely sensed data have been used widely for investigating global variability in Chl-a [22], frontal activities [15,17], dynamics of mesoscale eddies [25,29] and assessing water quality [47,48]. To reduce the impact of cloud and land contamination, the data for areas within 5 km of the coast and the data for areas with clouds are discarded. The daily Chl-a data are logarithmically transformed due to their log-normal distribution [49]. The data have a high spatial resolution, which is important for resolving mesoscale dynamics, such as fronts and eddies [14,23,27], and their impact on marine productivity [24]. SST data have been widely used to determine the SST gradients and frontal activities to investigate oceanic processes and air-sea interactions [23]. The daily SST gradient is calculated for each pixel such that the zonal gradient (G_x) and meridional gradient (G_y) are first calculated as the ratio of the SST difference among the surrounding pixels following the Sobel operator:

$$G_x = \left[-1 \quad 0 \quad +1\right] \times \left[A(i-1,j) \quad A(i,j) \quad A(i+1,j)\right] \Big/ (2 \times d_x) \tag{1}$$

$$G_y = \begin{bmatrix} +1 \\ 0 \\ -1 \end{bmatrix} \times \begin{bmatrix} A(i,j+1) \\ A(i,j) \\ A(i,j-1) \end{bmatrix} \Big/ \left(2 \times d_y\right) \tag{2}$$

where $A(i,j)$ is the SST data with i and j denoting to the pixel number in the meridional and zonal directions, respectively, and d_x and d_y are the corresponding distances between successive pixels in the zonal and meridional directions, respectively, which vary with latitude. The total gradient (G) is then obtained using $G = \sqrt{{G_x}^2 + {G_y}^2}$, following Wang et al. [23].

Daily observations of the SSH are acquired from Archiving, Validation and Interpretation of Satellite Oceanographic data (AVISO), which are provided by the Copernicus Marine Service (CMEMS). Please refer to the acknowledgements section for detailed information on data availability. The SSH data are obtained from altimetry observations, and the SLA is defined as the difference between the daily SSH and the corresponding climatology, which is calculated as the daily averaged SSH between 1993 and 2010. The spatial resolution is $0.25^{\circ} \times 0.25^{\circ}$, and the dataset has been widely used to identify mesoscale eddies in the global ocean and other dynamic processes [25]. Daily reanalyzed wind data are obtained from ERA-Interim products, a global atmospheric reanalysis developed by the European Centre for Medium-Range Forecasts (ECMWF). The spatial resolution is consistent with SLA observations at 0.25°, and there is no existing gap in the dataset. Detailed information regarding the reanalysis data can be found in Dee et al. [50].

The time period used in this study is from October 2002 to September 2018, and the time series for all parameters are calculated as monthly averages. Monthly averaging can effectively fill the gaps in the SST and Chl-a data without interfering with the underlying seasonal and interannual variability [23]. Seasonal averages of each parameter

are subsequently calculated for winter (January–March), spring (April–June), summer (July–September) and fall (October–December) using the monthly time series. The monthly climatology is obtained as the average for the corresponding month over 16 years calculated from the monthly averaged observations.

The vertical distribution of ocean features is important for understanding regional dynamics. The vertical profile of temperature is obtained from the World Ocean Atlas (2018) with a spatial resolution equal to 1° [51]. The data describe the monthly climatological temperature distribution by merging multiple sources of observations, including oceanographic casts from Argo and in situ observations [52]. There are 57 vertical layers for describing the temperature at each depth down to a depth of 5500 m, and the MLD is calculated as the depth at which the temperature is 0.8 °C less than that at the surface [53]. Different definitions of the MLD have been utilized in previous studies, and the selected method is found to be the most applicable for the study region, which ranges between 30° N and 39° N and between 130° E and 175° E (Figure 1). Please note that the area within this range that is located to the west of Japan is excluded from the current study.

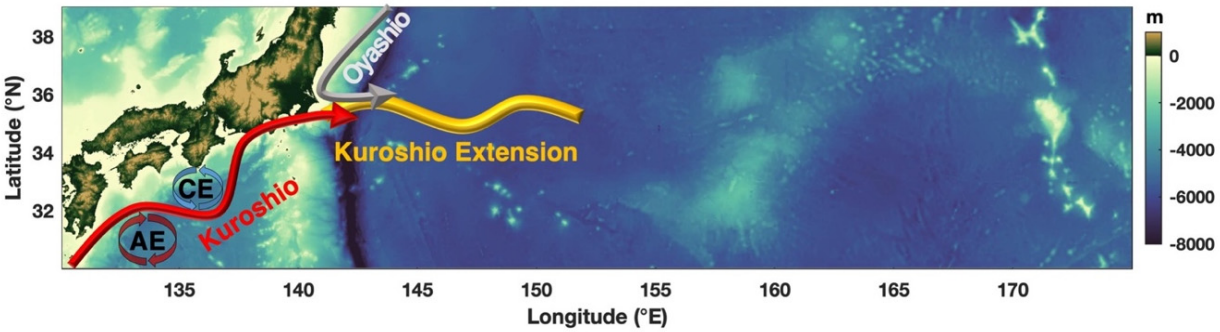


Figure 1. Topography (m), currents and major dynamic processes in the Kuroshio extension (KE) region. The major bathymetric features with shallow topography are the Izu-Ogasawara Ridge (139.7° E), the Shatsky Rise (159.8° E) and the Emperor Seamount (171.4° E). The schematic cyclonic (CE) and anticyclonic (AE) circulations that are frequently present to the south of Japan are labeled [1].

3. Results

3.1. Mean Field and Seasonal Variability of Major Features in the Kuroshio Extension

The water depth in the northwestern Pacific Ocean is generally deep, the majority of the region is deeper than 3000 m, and the coastal region that is less than 300 km from the coastline has depths less than 1000 m (Figure 1). There is a submarine ridge, i.e., the Izu-Ogasawara Ridge, that originates from central Japan (35.6° N, 139.7° E) and extends toward the south, where it is associated with a few islands. The largest depth is found immediately east of the ridge, where the depth can reach more than 8000 m. There are two other submarine ridges located to the east, i.e., the Shatsky Rise and the Emperor Seamount. The Kuroshio current and Oyashio current are schematically shown in Figure 1, together with the KE. The meander of the Kuroshio current can induce intense dynamic processes, such as mesoscale eddies, along the main stream of the Kuroshio current [12,25]. Because of the curvature of the Japanese coast and the shallow bathymetry around the Izu-Ogasawara Ridge, the meander and southward meridional flow of the Kuroshio current can induce relatively stable cyclonic and anticyclonic circulation to the south of Japan [40], which are schematically denoted by CE and AE, respectively (Figure 1). The large EKE of the KE can generate a great number of eddies and fronts [36], similar to other western boundary current systems [25]. It is important to point out that the stability of the KE [41] exhibits large interannual variability that is not captured in the figure.

The overall average SST ranges between 16 °C and 24 °C generally decrease northward (Figure 2a), particularly in the open ocean. In the coastal region, the Kuroshio current shows a prominent warm signal that originates from the southwest and is distributed along

the coast up to the east of Japan. Additionally, the cold Oyashio current can be identified to the northeast of Japan, and it is distributed along the coast southward until it converges with the Kuroshio current to the east of Japan. Consistently, the averaged Chl-a in the open ocean shows a prominent meridional dependence, with larger values in the north and smaller values in the south. The region with Chl-a values less than -0.8 $\log_{10}$ (mg/m^3) is characterized by low productivity [54]. Chl-a monotonically increases toward the coast and is especially high in the region northeast of Japan, where the value can be greater than -0.4 $\log_{10}$ (mg/m^3). The general dependence between SST and Chl-a is that high Chl-a are associated with low temperatures, which is consistent with the findings of previous studies [24]. Clearly, Chl-a are much higher in the Oyashio current than in the Kuroshio current.

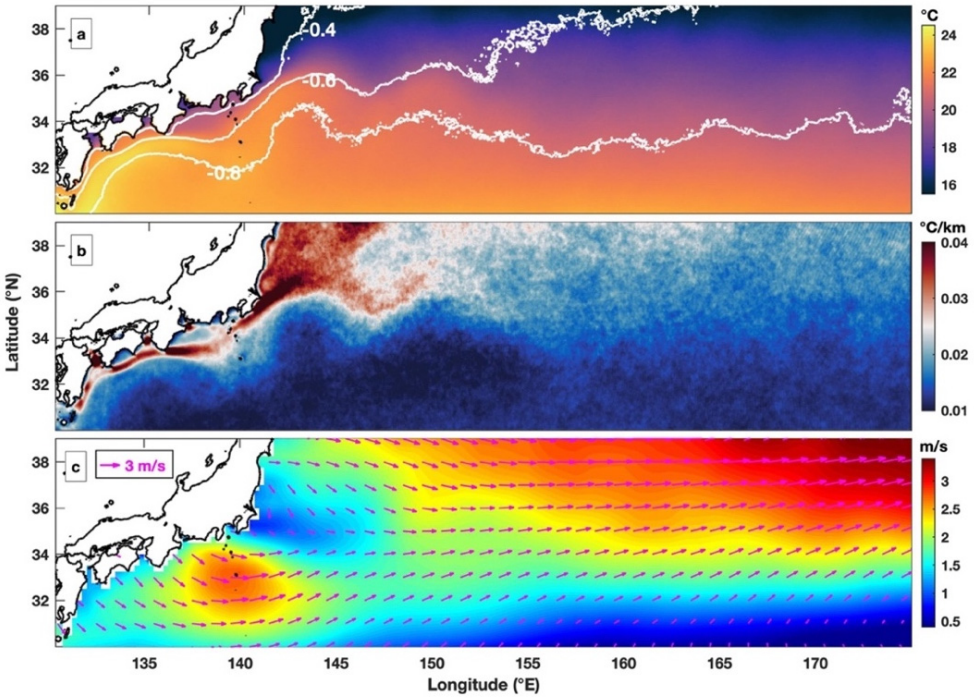


Figure 2. (**a**) Averaged sea surface temperature (SST, °C) overlaid with contours of the averaged Chl-a ($\log_{10}$ (mg/m^3)), (**b**) the averaged SST gradient (°C/km), and (**c**) the averaged wind speed magnitude (shading) overlaid with wind vectors in the KE region.

The mean SST gradient is very weak south of the Kuroshio current and KE (Figure 2b), and the corresponding value is less than 0.02 °C/km. A large SST gradient is found at the northern boundary of the Kuroshio current, where a large difference in SST is generated between the cold coastal surface water and the warm current, which is consistent with previous findings [55]. It is interesting to note that the corresponding high SST gradient, which is 0.03 °C/km or larger, is limited to only a narrow band near the coast, approximately 100 km offshore. A high SST gradient occupies a much larger zonal extent in the north, where the region is dominated by the Oyashio current and KE. In particular, the high SST gradient, e.g., 0.03 °C/km, in the KE extends more than 1000 km from the coast to the open ocean. The SST gradient has been widely used as an indicator for detecting sea surface fronts, and the applied threshold to define fronts is approximately 0.03 °C/km at mid-latitudes [15]. Thus, the KE region possesses abundant and intense frontal activities. The region with a high large averaged SST gradient is generally associated with a large temporal standard deviation as well (not shown) because of the strong seasonal and interannual variability in the KE. A comparison of the SST, Chl-a and SST gradient data shows a clear pattern related to the meander of the KE, exhibiting a curved pattern in the corresponding distributions, and their spatial locations are highly similar.

The wind field is mostly characterized as westerly for the entire region (Figure 2c). For the offshore region, the wind speed is generally greater in the north than in the south, and a weak convergence can be identified between 34° N and 38° N as the northward component of wind decreases toward the north. In the region close to Japan, the wind field is mostly blowing toward the southeast perpendicular to the coastline, with a large variance in direction. The intensity of wind is clearly influenced by the orography, as the wind speed is reduced to the leeward side of the main island, e.g., 36° N, 142° E, and intensified among mountain gaps, e.g., 33° N, 139° E.

The variability in the SST and Chl-a is further studied using their seasonal averages (Figure 3), and prominent seasonal differences are identified in both parameters. During winter (Figure 3a), the SST is between 10 °C and 20 °C, which is the lowest throughout the year, and the Kuroshio current clearly delivers warm water to high latitudes near the coast of Japan. Simultaneously, the spatially averaged Chl-a over the entire region reaches the annual maximum. This phenomenon is particularly true for the region to the south of the KE where the Chl-a values are greater than -0.7 $\log_{10}$ (mg/m^3) at all locations. In spring (Figure 3b), the transport of warm water by the Kuroshio current is still prominent since the surrounding water is cold (less than 22 °C). The Chl-a values in the south are generally lower in spring than in winter, except in the coastal area that are characterized by cyclonic and anticyclonic circulation (CE and ACE), as shown in Figure 1. Conversely, the Chl-a values impacted by the Oyashio current are clearly large in winter and reach the annual maximum of -0.2 $\log_{10}$ (mg/m^3). As the SST in the entire region peaks in summer (Figure 3c), the Kuroshio current can hardly be distinguished because the surroundings are also warm (26 °C or higher). In fall, all the factors show a transitional pattern in which SST decreases (Figure 3d) and Chl-a increases compared with the values in summer.

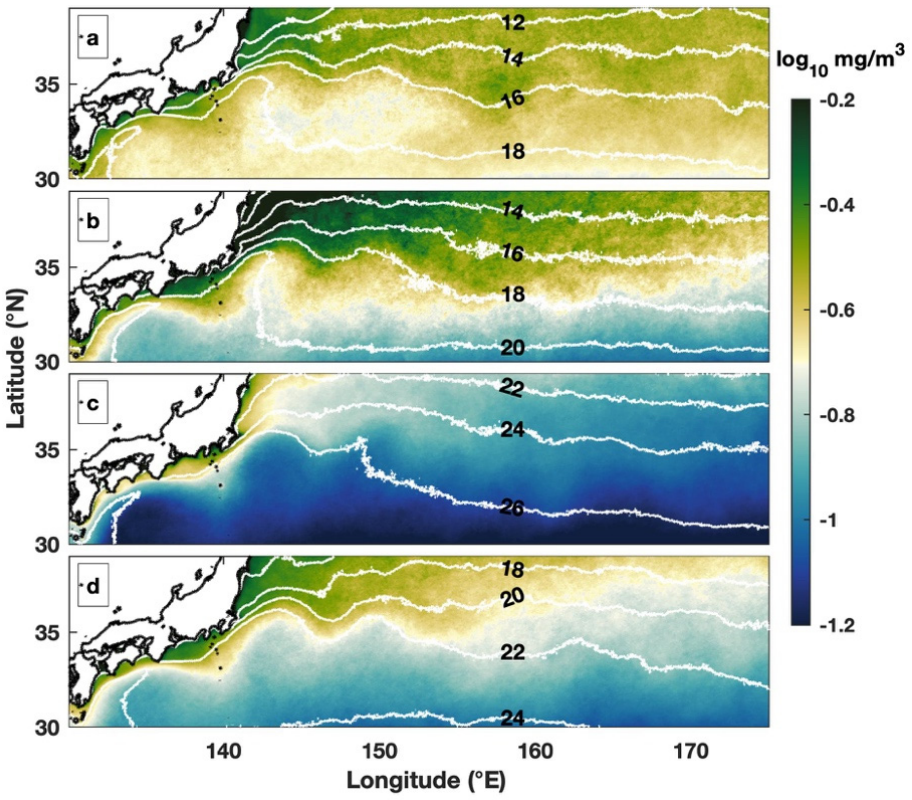


Figure 3. Seasonally averaged Chl-a ($\log_{10}$ (mg/m^3)) overlaid with SST (°C). The seasons are (**a**) winter (January–March), (**b**) spring (April–June), (**c**) summer (July–September), and (**d**) fall (October–December).

The seasonal variability in the SST gradient is prominent (Figure 4), although the general spatial pattern, e.g., the meridional difference, is consistent with the annual average. The SST gradient is high for the entire region during winter, especially in the northern section along the Oyashio current, and the corresponding peak value can be as high as 0.05 °C/km (Figure 4a). To the south of KE, the value is much lower, e.g., 0.01 °C/km or less. During spring, the SST gradient in the majority of the region reaches an annual maximum, especially around the Oyashio current and along the meander of the Kuroshio current (Figure 4b), which is consistent with the large SST changes during the same period (Figure 3b). In summer, the SST gradient (Figure 4c) generally decreases, especially in the Oyashio current where the value reaches the lowest value throughout the year (Figure 4c). This phenomenon is largely attributed to the warm SST over the entire region (Figure 3c). The SST gradient increases in autumn, acting as the transitional period between summer and winter (Figure 3d).

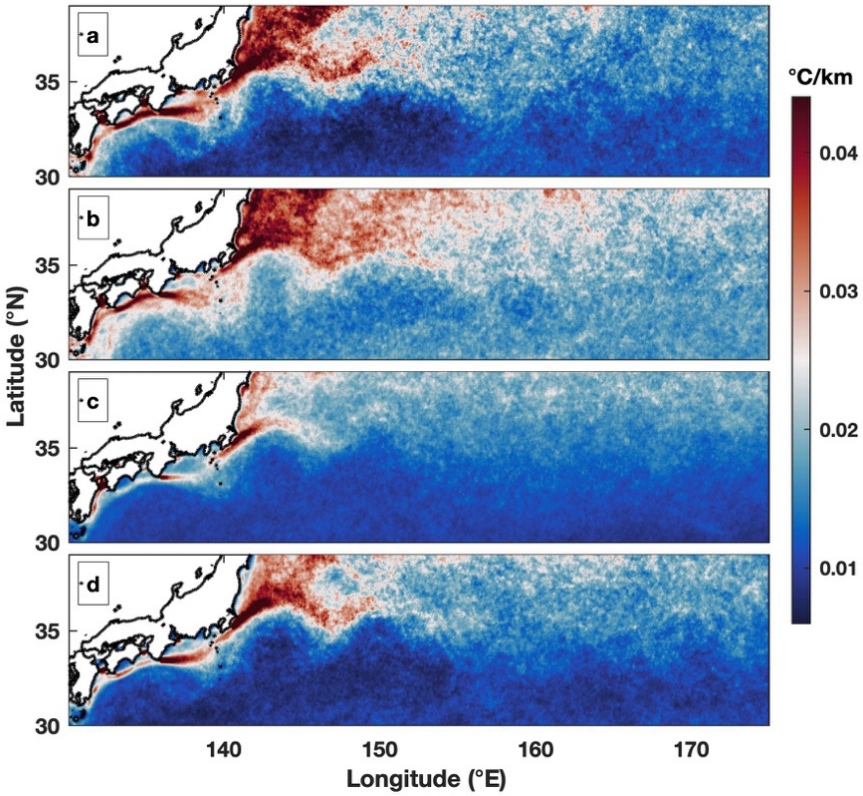


Figure 4. Seasonal variability of the sea surface temperature (SST) gradient (°C/km). The seasons are (**a**) winter (January–March), (**b**) spring (April–June), (**c**) summer (July–September), and (**d**) fall (October–December).

Wind speed also shows a clear seasonal variance after removing the overall average from the seasonal average (Figure 5). During boreal winter, the wind near the coast and in the northern section is intensified toward the northeast and southeast, respectively (Figure 5a). In particular, the wind speed reaches the annual maximum over the Oyashio current and remains highly consistent with the annual average over the Kuroshio current and the majority of the KE. In spring, the wind speed is weakest over the entire region (Figure 5b), especially for the region along the Kuroshio current. Please note that the range of shading and the unity wind vector in Figure 5 differs from that in Figure 2c, and the change in wind is generally weaker than the overall average. Thus, the negative value of wind change can be related to the reduced magnitude and change in direction. The strongest wind can be identified during the summer (Figure 5c), when the wind direction is generally consistent with the overall average but acts to intensify the wind field. This

phenomenon is particularly true for the KE, where the wind intensifies the mean wind field, which can be attributed to the warm Kuroshio current (Figure 3c) that reduces the stability of the atmospheric boundary layer and increases the wind fields [16]. The wind pattern in fall shows a cyclonic feature over the entire region east of Japan (Figure 5d), e.g., intensified southeastward wind to the south of Japan, northward component to the east (between 150° E and 160° E) and southwestward wind over the Oyashio current. Similar to other features, the wind in fall also acts as a transitional phase due to the corresponding small magnitude in the wind changes.

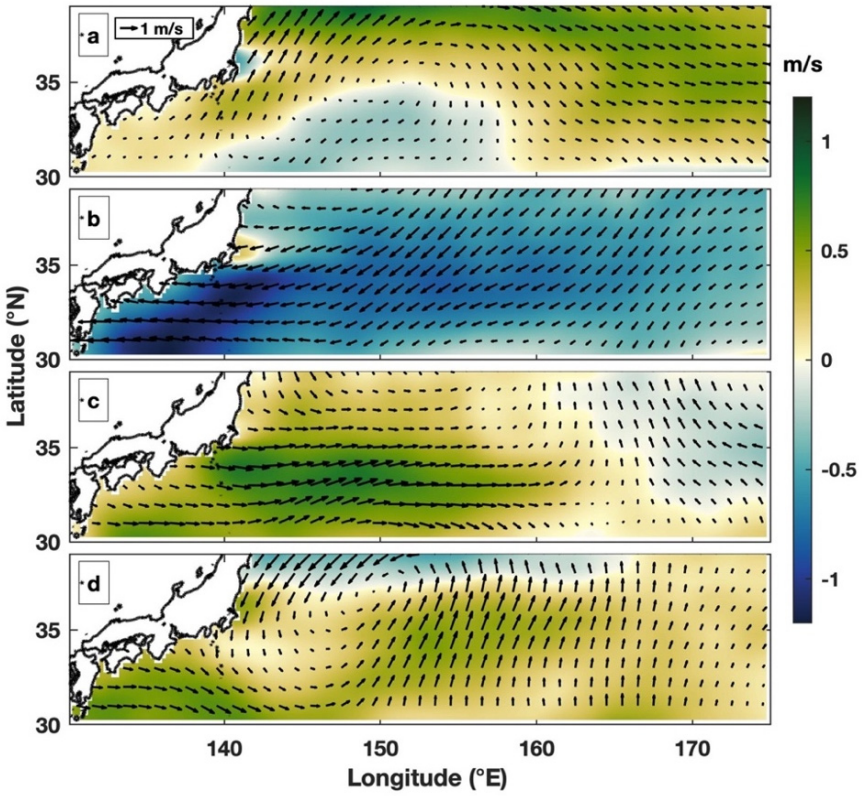


Figure 5. Seasonal changes in wind speed (shading) overlaid with the wind vector (m/s). The seasonal changes are obtained by removing the annual average from the seasonal average. The seasons are (**a**) winter (January–March), (**b**) spring (April–June), (**c**) summer (July–September), and (**d**) fall (October–December).

3.2. Dynamic Relationship among Factors in the Kuroshio Extension

The dynamics influencing the variability of Chl-a are further investigated in an anomalous field, which is obtained using the monthly time series and removing the overall average for the corresponding month, e.g., climatological monthly average. The time series of the Chl-a anomalies and SST gradient anomalies (Figure 6) are positively correlated in the meander of the Kuroshio current and upstream of the KE [8], where the correlation is significant at the 95% confidence level. The confidence level is determined by comparing the correlation with a threshold critical value of 0.28, which is calculated based on the degrees of freedom of the independent observations [15]. Different leads and lags are applied to the time series of the SST gradient and Chl-a data to identify potential lead–lag relationships, and the largest correlation is obtained when both time series are simultaneous. Thus, when the SST gradient anomaly in the main stream of the Kuroshio current and the center of the KE (Figure 1) is large (small), the corresponding Chl-a anomaly is high (low). The region where the variability in Chl-a is related to the SST gradient is precisely delineated in Figure 6, and its boundary in the north–south (east–west) direction is shown as dashed cyan (solid blue) lines. Meridionally, the boundary is defined as the

range within one standard deviation of the meridional variation from the center. In its western section, i.e., west of 142° E, the region lies roughly between 100 km and 300 km from the coast, and the coastal area is characterized by a low correlation. In the eastern section, the correlation is especially large within the KE and gradually decreases eastward. It should be noted that the location of the center of the region with the largest correlation in the meridional direction is also identified to the west of 134° E and to the east of 149° E, but the corresponding correlation is not significant.

Table 1. The correlation coefficient between the monthly time series of chlorophyll concentrations (Chl-a) and different parameters in climatological and anomalous fields for the enclosed region shown in Figure 6. The anomalous field is obtained using the monthly time series by removing the overall average for the corresponding month. The number in the bracket indicates the number of months for the parameter to obtain the correlation with Chl-a with the largest magnitude, where a positive (negative) value indicates the parameter is leading (lagging) the variability in Chl-a. The dash symbol indicates that the correlation is not significant at the 95% confidence level. Because mixed layer depth (MLD) is obtained as a monthly climatology, the correlation in the anomalous field is not available.

Parameters	Climatology	Anomaly
Sea surface temperature (SST)	−0.92 (0)	−0.22 (-)
SST gradient	+0.92 (−1)	+0.51 (0)
Sea level anomaly (SLA)	−0.81 (−1)	−0.57 (0)
MLD	+0.87 (+2)	-

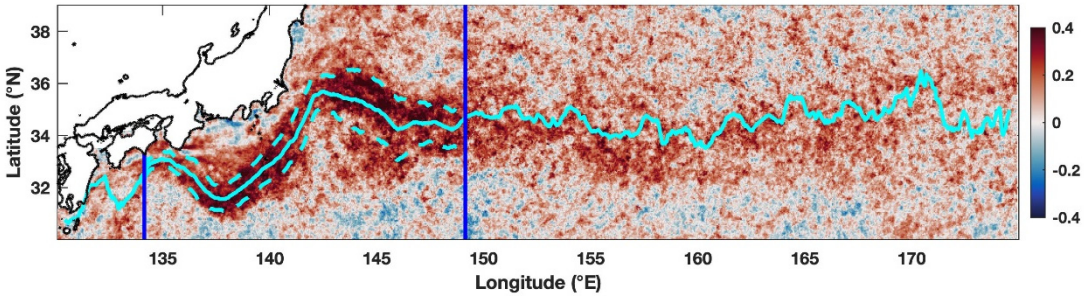


Figure 6. Correlation between the time series of the SST gradient and Chl-a in the anomalous field. The correlation is significant at the 95% confidence level if the critical value is greater than and less than 0.28 and −0.28, respectively. The solid (dashed) cyan line represents the location of the center (boundary) of the region with a large correlation, >0.28, in the meridional direction. The boundary is defined as the range within one standard deviation of the meridional variation from the center. The solid blue lines represent the averaged boundary of the region with a significant correlation in the zonal direction. The region with a significant correlation is used to obtain Figures 7–9 and Table 1.

The variability in Chl-a and other factors in the meander of the Kuroshio current and upstream of the KE, which is characterized by a significant correlation in Figure 6, is investigated to assess the seasonal variability (Figure 7). Prominent seasonal cycles are identified in the climatological monthly average of all the factors; for example, Chl-a peaks in April and rapidly decreases until August before increasing again (Figure 7a). Previous studies have revealed that the variability in Chl-a is related to the SST and MLD during the seasonal cycle [24] and that locally high Chl-a values occurs in local winter in association with a low SST and deep MLD. In the current study, the monthly time series consistently captured a low SST and deep MLD in winter (Figure 7b). A significant negative correlation is found between SST and Chl-a (Figure 7b), and the largest correlation occurs when the SST variations are simultaneous with Chl-a; a significant negative correlation is also found between MLD and Chl-a, and the largest correlation occurs when MLD leads Chl-a by two months. Additionally, the SST gradient also shows a distinctive seasonal cycle, peaking in April and May and then decreasing rapidly until August (Figure 7c). The variability in

Chl-a and the SST gradient are highly consistent with each other, with the SST gradient slightly lagging by one month, indicating that the oceanic dynamics are important for driving the seasonal variability in Chl-a. The dependence between Chl-a and other factors during the climatological seasonal cycle is summarized in Table 1.

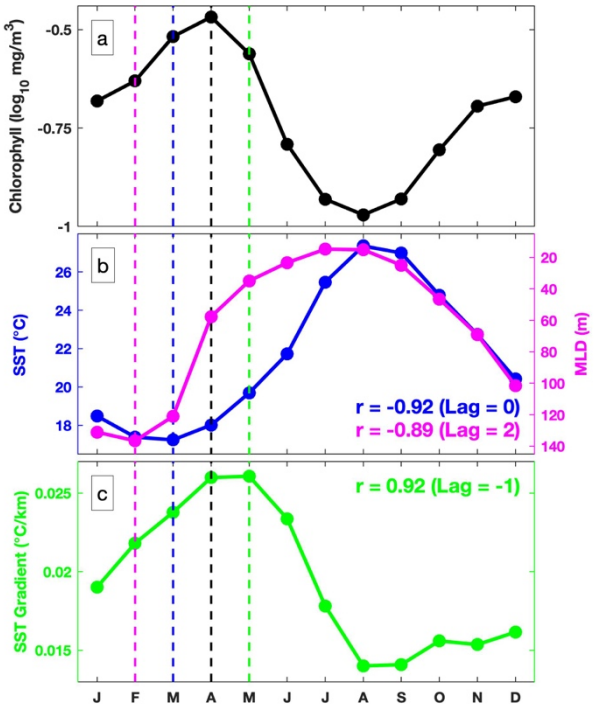


Figure 7. Monthly averaged (**a**) Chl-a ($\log_{10}$ (mg/m^3)), (**b**) SST (blue, °C) and MLD (magenta, m), and (**c**) SST gradient (°C/km). The vertical dashed lines represent the annual peaks for Chl-a (black) and SST gradient (green) and annual troughs for SST (blue) and MLD (magenta). The correlation between Chl-a and other factors and the associated lag to obtain the largest correlation are labeled in the corresponding panels, where a positive (negative) value indicates that the parameter is leading (lagging) the variability in Chl-a.

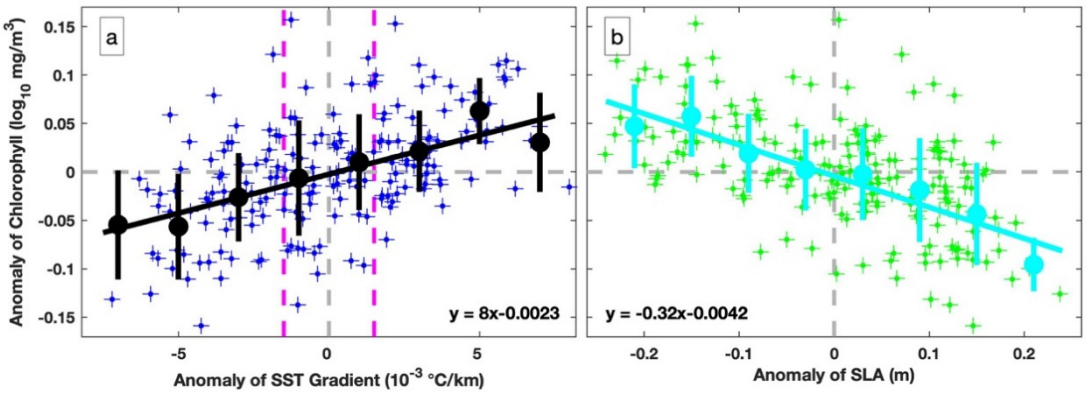


Figure 8. Scatterplots of Chl-a ($\log_{10}$ (mg/m^3)) versus (**a**) SST gradient (°C/km) and (**b**) SLA (m) in the anomalous field. In (**a**), black dots are the averaged Chl-a for each bin of the SST gradient, with vertical bars representing the corresponding standard deviation. Similarly, in (**b**), cyan dots are the averaged Chl-a for each bin of SLA. The solid lines are obtained using linear regression between the values of bins and bin-averaged Chl-a, and both of them are significant at the 95% confidence level. The obtained regression is labeled in the corresponding panel. Dots between the magenta dashed lines in (**a**) represent small magnitudes of the SST gradient.

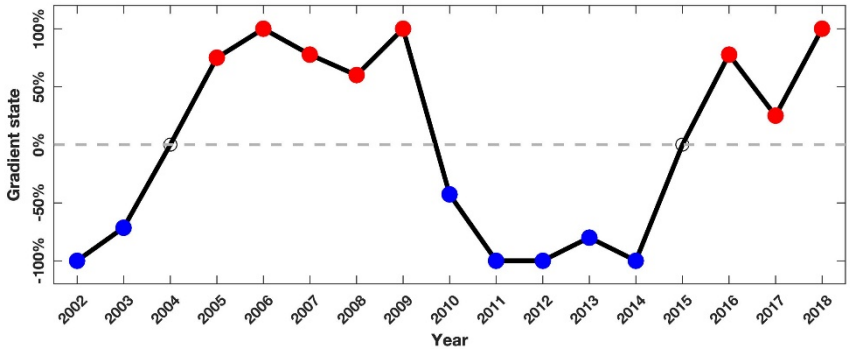


Figure 9. Gradient state based on the annual percentage of the anomaly in the SST gradient magnitude. Red (blue) dots indicate a high percentage of large positive (negative) anomalies in SST gradient magnitudes. The dashed gray line represents the percentage where the positive and negative SST gradient magnitudes are equal, with hollow dots indicating a neutral state. If more than 50% of the time in a year the month is characterized as a near-zero anomaly in SST gradient magnitude, the corresponding year is also defined as a neutral state.

The impact of major dynamic processes on Chl-a, such as those indicated by the SST gradient and SLA, is further quantified in an anomalous field for the region delineated in Figure 6. The SST gradient magnitude (Figure 8a) and SLA (Figure 8b) are divided into eight bins, and the corresponding Chl-a is averaged for each bin. The relationship is clearly captured from their scatterplots showing that abnormally high Chl-a values are associated with a positive anomaly in SST gradient magnitude and a negative anomaly in SLA. It should be noted that no lag is applied since the largest correlation is obtained when the time series are simultaneous (Table 1). Because the correlation between SST and Chl-a is not significant (Table 1), the corresponding information is not included in the figure. Linear regressions are applied using the bin-averaged values of the SST gradient magnitude and SLA and the bin-averaged Chl-a to gauge the dependence of Chl-a on these factors, and the acquired regression coefficients are significant at the 95% confidence level [15]. This method offers a quantitative approach to estimate the change in Chl-a based on oceanic processes. The applied linear regression does not imply that the dependence is linear, but it can be used as an indicator to estimate the Chl-a anomalies that are induced by certain processes and to compare Chl-a values at different times. The SST gradient is further applied to represent the state of the ocean, and three groups are separated based on their SST gradient magnitude anomalies. The groups are defined as those with large negative anomaly values ($<-1.5\times10^{-3}$ °C/km), large positive anomaly values ($>1.5\times10^{-3}$ °C/km) and those with anomaly values close to zero. There are roughly the same number of SST gradient magnitude anomalies in each group. The groups of SST gradient magnitudes are useful for defining the dynamic state of the KE, which will be explained in the following paragraph. It should be noted that there is no significant dependence between the wind field and Chl-a in either the climatological or anomalous fields, which might be because the wind is determined by large-scale atmospheric circulation and modified by mesoscale air-sea interactions [56], but has little influential on regional dynamics and Chl-a variability. Thus, the corresponding relationship between wind and Chl-a is not included in this study.

3.3. Impact of Kuroshio Extension Stability on Modulating Oceanic Features

The anomaly of SST gradient magnitude in each month can be classified into one of the three groups depending on its value, e.g., large positive, large negative and the remaining with small magnitude. Then, the ratio between the difference in the number of months with large anomaly values (i.e., the number of months with large positive values minus the number of months with large negative values) and the number of months excluding those with a small magnitude is obtained for each year (Figure 9). Here, a positive (negative) ratio indicates more months characterized by anomalously large (small) SST gradient magnitude within the year. Prominent interannual variability is identified in which a

positive (negative) gradient state occurs between 2005 and 2009 and after 2016 (before 2003 and between 2010 and 2014). Only two years, 2004 and 2015, are characterized by a neutral state with the same number of months with anomalously large and small SST gradient magnitudes, or more than 50% of months are characterized as near-zero magnitude of SST gradient anomalies within a year. Thus, the switch between different states occurs in a rapid manner, and each state can be maintained for a few years. Comparing the time series with the previously identified stability of the KE [39], a clear dependence is identified between the stability of the KE and the SST gradient state. A positive (negative) anomaly in the SST gradient magnitude is generally associated with the unstable (stable) mode of the KE, and the gradient state leads by one or two years. Thus, the state of the SST gradient magnitude can be applied as an index to predict the interannual variability in the stability of the KE in the following years.

The SST gradient states described above are used to investigate the changes in the KE during different states. The SST gradient, Chl-a, SLA and wind field are individually averaged in each pixel for the period when the anomaly of SST gradient magnitude is large, either with a positive or a negative value. The difference for each factor is obtained by subtracting the average during the period with a large negative gradient state from the average during the period with a large positive gradient state (Figure 10). A clear positive dependence can be observed between the SST gradient magnitude and Chl-a in the anomalous field (Figure 8a). Thus, a predominantly positive SST gradient magnitude and Chl-a are found for the identified region (Figure 10a,b). Consistently, the negative dependence between SLA and Chl-a in the anomalous field (Figure 8b) is revealed as the negative difference in SLA (Figure 10c). For all the features, the difference is much weaker in the western section, which is the meander of the Kuroshio Current, than in the eastern section, which is upstream of the KE. The wind speed is intensified over the identified region (Figure 10d) with a prominent northward component, although the wind speed actually decreases near shore and in the north. Noticeably, the difference in the SST gradient magnitude is found only within the identified region, but the difference in Chl-a, SLA and wind extends farther along the meander of the KE with a similar spatial pattern and is associated with a decrease in magnitude until fading occurs near 158° E. As the SST gradient state becomes positive and large upstream of the KE due to the increasing instability of the KE, the corresponding Chl-a and wind values increase, while the SLA decreases throughout the KE.

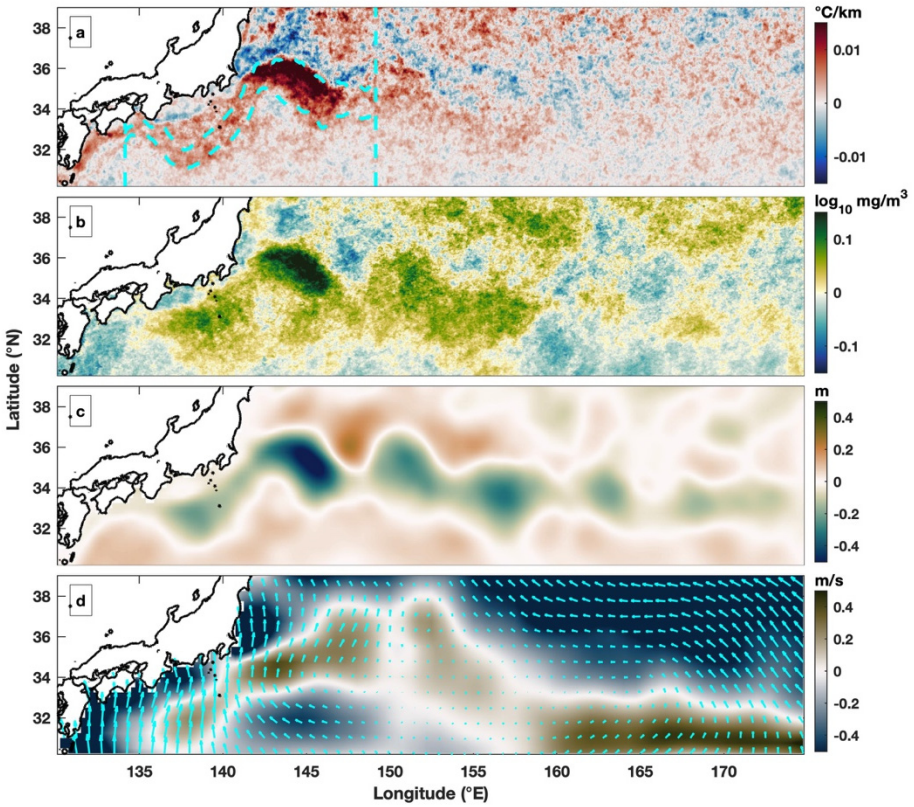


Figure 10. Differences in the (**a**) SST gradient magnitude, (**b**) Chl-a, (**c**) SLA, and (**d**) wind speed overlaid with the wind vector between times when the SST gradient magnitude is abnormally large. The fields are obtained by subtracting the monthly average when the anomaly in the SST gradient magnitude is largely negative from the time when the large anomaly in the SST gradient magnitude is largely positive. The region used to obtain the SST gradient magnitude is shown as the area enclosed by the dashed cyan lines in (a), which is consistent with the region delineated in Figure 6.

4. Discussion

The current study focuses on the KE region, in the northwestern Pacific Ocean at mid-latitudes, where the upper ocean is characterized as highly dynamic with prominent variability. The supply of nutrients via dynamic processes can enhance the growth of phytoplankton and subsequently increase Chl-a [57], in contrast to coastal regions where nutrients are persistently high [58]. The KE region is characterized by predominant seasonal variability in major features, e.g., Chl-a, SST, SST gradient and wind field. The seasonal cycle of different factors captures a clear dependence of Chl-a on regional oceanic dynamics. For instance, high Chl-a occurs in winter and spring when the deep MLD introduces nutrients from the subsurface into the euphotic zone, thereby enhancing the growth of phytoplankton [31]. In particular, the peak of Chl-a during spring (Figures 3b and 7a) is consistent with the spring bloom identified in previous studies, when shoaling of the MLD and increasing light intensity stimulate the growth of phytoplankton [59,60]. The corresponding wind is actually weak over the Kuroshio current and KE, indicating that wind is not a factor driving the increase in Chl-a [24].

A detailed investigation found that high Chl-a in the study area (Figure 3) were initially identified in the west at 134° E in March and gradually migrated eastward to 150° E within one month (not shown), yielding a propagation speed of approximately 0.65 m/s, which is consistent with previous observations [61]. During the same period, the high SST gradient indicates active ocean dynamics, e.g., fronts and eddies, which can aggregate and transport nutrients in the upper ocean and subsequently increase Chl-a [37]. It is important to note that the monthly time series of the MLD leads that of Chl-a by two months and the monthly time series of the SST gradient lags that of Chl-a by one month (Figure 7). Previous

studies have identified that the factors usually vary simultaneously [24], but in the KE, the seasonal cycles of the MLD and SST gradients are slightly different, and the subsequent variability in Chl-a varies between them (Figure 7). This is likely due to the biological responses lagging the dynamic processes by several days, i.e., the time required for the growth of phytoplankton [62]. The SLA represents the vertical processes and a negative (positive) value is associated with local upwelling (downwelling) [27–29] that increases (decreases) the nutrient content in the upper ocean [31]. Consistently, Sasai et al. [33] found that cyclonic eddies, which are characterized by low SLAs [25], elevate high-nutrient subsurface water into the euphotic zone and result in high Chl-a even in summer; thus, a significant correlation is persistently found between SLA and Chl-a in anomalous fields (Figure 8b).

Most parameters are characterized by seasonal variability [63], which can always be correlated with each other with certain lags [64], although there is no valid underlying dynamic relationship. The anomalous field, which is calculated by removing the seasonal or annual cycles [15], is subsequently investigated because it can effectively increase the number of independent observations [65] to obtain a solid relationship. Although the entire KE region is dynamically energetic, only the captured zone is characterized by a significant correlation between the SST gradient and Chl-a in the anomalous field (Figure 6). When upwelling or mixing is anomalously large [24], the SST gradient increases, the SLA decreases, and substantial nutrients are transported from the subsurface into the upper layer [66], leading to a simultaneous increase in Chl-a (Figure 8). Indeed, the major marine features are dynamically bound to each other, and it is important to remove the seasonal cycle to reveal the underlying relationships.

Prominent interannual variability is identified in the SST gradient, and the period with a large SST gradient indicates more instability during this period. An index of the SST gradient is defined in the current study based on the magnitude of the SST gradient anomaly over a year (Figure 8). The determined period with a large or small gradient state (Figure 9) is consistent with the stability of the KE identified in previous studies [32], but the change in gradient state leads by one to two years in the current study. Thus, the SST gradient state can be used as an indicator for forecasting the stability of the KE and predicting Chl-a in the region. A significant correlation is identified between the SST gradient index and annually averaged PDO [41], with the latter leading by two years, and the corresponding correlation coefficient equals 0.74. A significant correlation is also identified between the SST gradient index and annually averaged NPGO, with the NPGO leading by one year and a corresponding correlation coefficient of -0.62. This phenomenon reveals that the large-scale climatic pattern in the eastern Pacific Ocean can impact the northwestern Pacific Ocean, and the lag indicates the time required for the signal to propagate across the ocean basin [43].

There are other oceanic features that can be used to indicate regional dynamic processes, which are not incorporated in the current study. For example, the EKE is widely used to describe regional dynamics [67], where a high (low) EKE is identified during the period when the KE is unstable (stable) [38]. The EKE can be calculated using the geostrophic current, which is usually obtained using the field of SLAs [36]. A negative (positive) SLA may indicate a cyclonic (anticyclonic) eddy in the surrounding region if there is a closed SLA contour [28]. Thus, an eddy-induced EKE can be gauged using SLAs, and a large SLA, regardless of whether it is positive or negative, indicates strong eddy activity [25]. In the current study, we are particularly interested in cyclonic eddies because induced upwelling can transport nutrients and mix the subsurface Chl-a maximum (SCM) into the upper layer [29]. Because the number of cyclonic eddies is approximately consistent with that of anticyclonic eddies in the KE, a small SLA can represent few eddies of both polarities and low magnitude of the EKE in general, and vice versa [36].

Additionally, the wind stress is highly correlated with SST at the mesoscale, and high (low) SST is associated with strong (weak) winds [56], as identified in the current study (Figures 3 and 5). As wind blows perpendicular to the SST gradient, it generates

a wind stress curl [68] that can, in turn, supply feedback to the distribution of SST in the KE via Ekman pumping [69], leading to a fully coupled air-sea system [70]. Wind can impact the variability in Chl-a by Ekman pumping of subsurface water [24] and influence vertical mixing [71]. Corresponding information is incorporated in the seasonal cycle of MLD (Figure 7b) and changes in the SST gradient anomaly (Figure 8a), although a direct significant correlation between wind and Chl-a is not identified. Thus, the underlying dynamics of wind among other factors are related to those of the incorporated factors, and the effects of these other factors are already considered in the applied features.

Remote sensing data effectively and accurately capture ocean surface features in dynamic regions [72]; however, subsurface information is not incorporated. For example, the fronts in the KE can extend to a depth of more than 300 m, where large anomalies can be identified in the temperature and other features [73,74]. Additionally, even in areas where Chl-a is low at the surface, a subsurface Chl-a bloom can be identified by a profiling float equipped with biogeochemical sensors [66,75]. Compared with surface Chl-a, the integrated Chl-a within the euphotic zone shows less prominent seasonal variability throughout the year [60]. Three-dimensional observations in the future could help more fully describe the physical and biological status of the ocean.

5. Conclusions

Sixteen years of satellite observations of the KE are used to investigate the regional dynamics and their impact on modulating the variability in Chl-a. As a typical mid-latitude area, the seasonal cycle dominates the entire region, which is revealed by the distinctive seasonal pattern in Chl-a. The seasonal variability in Chl-a is simultaneously modulated by the horizontal and vertical structures of water masses, which are delineated by the SST gradient and MLD, respectively. The underlying influence of dynamic processes, e.g., fronts and eddies, on Chl-a is confirmed in the anomalous field in which a significant correlation between Chl-a and other factors is identified only upstream of the KE. The SST gradient for the area is used to indicate the dynamic status of the region and can further be used to predict the interannual variability in stability of KE and Chl-a. The current study offers a universally applicable method to investigate the impact of marine dynamics on Chl-a and other factors, and it can help assess the carbon cycle [76] and evaluate habitat for fishes and other high trophic level marine animals in global oceans.

Author Contributions: Visualization, funding, writing, Y.W.; investigation, data curation, R.T.; conceptualization, Y.Y.; review of the manuscript, F.J. All authors have read and agreed to the published version of the manuscript.

Funding: The study was funded by the National Natural Science Foundation of China [nos. 41806026, 41730536 and 41890805], the Project of State Key Laboratory of Satellite Ocean Environment Dynamics, Second Institute of Oceanography, MNR [no. SOEDZZ2102], the Oceanic Interdisciplinary Program of Shanghai Jiao Tong University and Scientific Research Fund of the Second Institute of Oceanography, MNR [no. SL2020ZD201].

Data Availability Statement: Sea surface temperature (SST) and sea surface chlorophyll-a (Chl-a) datasets are available from National Aeronautics and Space Administration (NASA) [77,78], the sea level data is obtained from the E.U. Copernicus Marine Service (CMEMS) (https://resources.marine.copernicus.eu/?option=com_csw&view=details&product_id=SEALEVEL_GLO_PHY_L4_NRT_OBSERVATIONS_008_046, last accessed on 16 October 2020), the ERA-Interim reanalysis product of wind is re-leased by the European Center for Medium-Range Weather Forecasts (ECMWF) (http://apps.ecmwf.int/datasets/data/interim-full-daily/levtype=sfc/, last accessed on 16 October 2020) [79], and the dataset of World Ocean Atlas is accessed from the National Oceanic and Atmospheric Administration (NOAA) (http://www.nodc.noaa.gov/, last accessed on 16 October 2020) [51].

Acknowledgments: We are very thankful to the shared code for providing the colormap to generates the figures [80].

Conflicts of Interest: The authors declare no conflict of interest.

References

1. Miyazawa, Y.; Zhang, R.; Guo, X.; Tamura, H.; Ambe, D.; Lee, J.S.; Okuno, A.; Yoshinari, H.; Setou, T.; Komatsu, K. Water mass variability in the western North Pacific detected in a 15-year eddy resolving ocean reanalysis. *J. Oceanogr.* **2009**, *65*, 737–756. [CrossRef]
2. Kawabe, M. Variations of current path, velocity, and volume transport of the Kuroshio in relation with the large meander. *J. Phys. Oceanogr.* **1995**, *25*, 3103–3117. [CrossRef]
3. Kagimoto, T.; Yamagata, T. Seasonal transport variations of the Kuroshio: An OGCM simulation. *J. Phys. Oceanogr.* **1997**, *27*, 403–418. [CrossRef]
4. Vivier, F.; Kelly, K.A.; Thompson, L. Heat budget in the Kuroshio Extension region: 1993–1999. *J. Phys. Oceanogr.* **2020**, *32*, 3436–3454. [CrossRef]
5. Imawaki, S.; Uchida, H.; Ichikawa, H.; Fukasawa, M.; Umatani, S.; ASUKA Group. Satellite altimeter monitoring the Kuroshio transport south of Japan. *Geophys. Res. Lett.* **2001**, *28*, 17–20. [CrossRef]
6. Watanabe, Y. Recruitment variability of small pelagic fish populations in the Kuroshio-Oyashio transition region of the western North Pacific. *J. North Atl. Fish. Sci.* **2009**, *41*, 197–204. [CrossRef]
7. Uehara, K.; Ito, S.; Miyake, H.; Yasuda, I.; Shimizu, Y.; Watanabe, Y. Absolute volume transports of the Oyashio referred to moored current meter data crossing the OICE. *J. Oceanogr.* **2004**, *60*, 397–409. [CrossRef]
8. Qiu, B. Interannual variability of the Kuroshio Extension system and its impact on the wintertime SST field. *J. Phys. Oceanogr.* **2000**, *30*, 1486–1502. [CrossRef]
9. Nakano, H.; Tsujino, H.; Hirabara, M.; Yasuda, T.; Motoi, T.; Ishii, M.; Yamanaka, G. Uptake mechanism of anthropogenic CO_2 in the Kuroshio Extension region in an ocean general circulation model. *J. Oceanogr.* **2011**, *67*, 765–783. [CrossRef]
10. Sakamoto, T.T.; Hasumi, H.; Ishii, M.; Emori, S.; Suzuki, T.; Nishimura, T.; Sumi, A. Responses of the Kuroshio and the Kuroshio Extension to global warming in a high-resolution climate model. *Geophys. Res. Lett.* **2005**, *32*, L14617. [CrossRef]
11. Kida, S.; Mitsudera, H.; Aoki, S.; Guo, X.; Ito, S.I.; Kobashi, F.; Komori, N.; Kubokawa, A.; Miyama, T.; Morie, R.; et al. Oceanic fronts and jets around Japan: A review. *J. Oceanogr.* **2015**, *71*, 469–497. [CrossRef]
12. Qiu, B.; Chen, S. Variability of the Kuroshio Extension jet, recirculation gyre, and mesoscale eddies on decadal time scales. *J. Phys. Oceanogr.* **2005**, *35*, 2090–2103. [CrossRef]
13. Yoder, J.A.; Ackleson, S.G.; Barber, R.T.; Flament, P.; Balch, W.M. A line in the sea. *Nature* **1994**, *371*, 689–692. [CrossRef]
14. Castelao, R.M.; Wang, Y. Wind-driven variability in sea surface temperature front distribution in the California Current System. *J. Geophys. Res. Oceans* **2014**, *119*, 1861–1875. [CrossRef]
15. Wang, Y.; Castelao, R.M.; Yuan, Y. Seasonal variability of alongshore winds and sea surface temperature fronts in Eastern Boundary Current Systems. *J. Geophys. Res. Oceans* **2015**, *120*, 2385–2400. [CrossRef]
16. Parfitt, R.; Czaja, A.; Minobe, S.; Kuwano-Yoshida, A. The atmospheric frontal response to SST perturbations in the Gulf Stream region. *Geophys. Res. Lett.* **2016**, *43*, 2299–2306. [CrossRef]
17. Chen, H.H.; Qi, Y.; Wang, Y.; Chai, F. Seasonal variability of SST fronts and winds on the southeastern continental shelf of Brazil. *Ocean Dyn.* **2019**, *69*, 1387–1399. [CrossRef]
18. Nagai, T.; Tandon, A.; Yamazaki, H.; Doubell, M.; Gallager, S. Direct observations of microscale turbulence and thermohaline structure in the Kuroshio Front. *J. Geophys. Res.* **2012**, *117*, C08013. [CrossRef]
19. Ribalet, F.; Marchetti, A.; Hubbard, K.; Brown, K.; Durkin, C.; Morales, R.; Robert, M.; Swalwell, J.; Tortell, P.; Armbrust, E. Unveiling a phytoplankton hotspot at a narrow boundary between coastal and offshore waters. *Proc. Natl. Acad. Sci. USA* **2010**, *107*, 16571–16576. [CrossRef]
20. Taylor, A.G.; Goericke, R.; Landry, M.R.; Selph, K.; Wick, D.; Roadman, M. Sharp gradients in phytoplankton community structure across a frontal zone in the California Current ecosystem. *J. Plankton Res.* **2012**, *34*, 778–789. [CrossRef]
21. Vantrepotte, V.; Mélin, F. Inter-annual variations in the SeaWiFS global chlorophyll a concentration (1997–2007). *Deep Sea Res. I* **2011**, *58*, 429–441. [CrossRef]
22. Mao, Z.; Mao, Z.; Jamet, C.; Linderman, M.; Wang, Y.; Chen, X. Seasonal Cycles of Phytoplankton Expressed by Sine Equations Using the Daily Climatology from Satellite-Retrieved Chlorophyll-a Concentration (1997–2019) Over Global Ocean. *Remote Sens.* **2020**, *12*, 2662. [CrossRef]
23. Wang, Y.; Yu, Y.; Zhang, Y.; Chai, F. Distribution and variability of sea surface temperature fronts in the South China Sea. *Estuar. Coast. Shelf Sci.* **2020**, *240*, 106793. [CrossRef]
24. Yu, Y.; Xing, X.; Liu, H.; Yuan, Y.; Wang, Y.; Chai, F. The variability of chlorophyll-a and its relationship with dynamic factors in the basin of the South China Sea. *J. Mar. Syst.* **2019**, *200*, 103230. [CrossRef]
25. Chelton, D.B.; Gaube, P.; Schlax, M.G.; Early, J.J.; Samelson, R.M. The influence of nonlinear mesoscale eddies on near-surface oceanic chlorophyll. *Science* **2011**, *334*, 328–332. [CrossRef]
26. Kouketsu, S.; Tomita, H.; Oka, E.; Hosoda, S.; Kobayashi, T.; Sato, K. The role of mesoscale eddies in mixed layer deepening and mode water formation in the western North Pacific. *J. Oceanogr.* **2012**, *68*, 63–77. [CrossRef]
27. Wang, Y.; Zhang, H.; Chai, F.; Yuan, Y. Impact of Mesoscale Eddies on Chlorophyll Variability off the Coast of Chile. *PLoS ONE* **2018**, *13*, e0203598. [CrossRef] [PubMed]
28. Gaube, P.; McGillicuddy, D.J.; Chelton, D.B.; Behrenfeld, M.J.; Strutton, P.G. Regional variations in the influence of mesoscale eddies on near-surface chlorophyll. *J. Geophys. Res. Oceans* **2014**, *119*, 8195–8220. [CrossRef]

29. He, Q.; Zhan, H.; Xu, J.; Cai, S.; Zhan, W.; Zhou, L.; Zha, G. Eddy-induced chlorophyll anomalies in the western South China Sea. *J. Geophys. Res. Oceans* **2019**, *124*, 9487–9506. [CrossRef]
30. Sun, B.; Liu, C.; Wang, F. Eddy induced SST variation and heat transport in the western North Pacific Ocean. *J. Oceanol. Limnol.* **2020**, *38*, 1–15. [CrossRef]
31. Dufois, F.; Hardman-Mountford, N.J.; Fernandes, M.; Wojtasiewicz, B.; Shenoy, D.; Slawinski, D.; Gauns, M.; Greenwood, J.; Toresen, R. Observational insights into chlorophyll distributions of subtropical South Indian Ocean eddies. *Geophys. Res. Lett.* **2017**, *44*, 3255–3264. [CrossRef]
32. Kouketsu, S.; Kaneko, H.; Okunishi, T.; Sasaoka, K.; Itoh, S.; Inoue, R.; Ueno, H. Mesoscale eddy effects on temporal variability of surface chlorophyll a in the Kuroshio Extension. *J. Oceanogr.* **2016**, *72*, 439–451. [CrossRef]
33. Sasai, Y.; Richards, K.J.; Ishida, A.; Sasaki, H. Effects of cyclonic mesoscale eddies on the marine ecosystem in the Kuroshio Extension region using an eddy-resolving coupled physical-biological model. *Ocean Dyn.* **2010**, *60*, 693–704. [CrossRef]
34. Enikeev, V.K.; Mikhailichenko, Y.G. On anticyclonic spin-off eddies in the Gulf Stream. *Soviet J. Phys. Oceanogr.* **1990**, *1*, 303–307. [CrossRef]
35. Spall, M.A. Generation of strong mesoscale eddies by weak ocean gyres. *J. Mar. Res.* **2000**, *58*, 97–116. [CrossRef]
36. Ji, J.; Dong, C.; Zhang, B.; Liu, Y.; Zou, B.; King, G.P.; Xu, G.; Chen, D. Oceanic eddy characteristics and generation mechanisms in the Kuroshio Extension region. *J. Geophys. Res. Oceans* **2018**, *123*, 8548–8567. [CrossRef]
37. Clayton, S.; Nagai, T.; Follows, M.J. Fine scale phytoplankton community structure across the Kuroshio Front. *J. Plankton Res.* **2014**, *36*, 1017–1030. [CrossRef]
38. Lin, P.; Chai, F.; Xue, H.; Xiu, P. Modulation of decadal oscillation on surface chlorophyll in the Kuroshio Extension. *J. Geophys. Res. Oceans* **2014**, *119*, 187–199. [CrossRef]
39. Qiu, B.; Chen, S.; Schneider, N.; Taguchi, B. A coupled decadal prediction of the dynamic state of the Kuroshio Extension system. *J. Clim.* **2014**, *27*, 1751–1764. [CrossRef]
40. Seo, Y.; Sugimoto, S.; Hanawa, K. Long-term variations of the Kuroshio Extension path in winter: Meridional movement and path state change. *J. Clim.* **2014**, *27*, 5929–5940. [CrossRef]
41. Qiu, B.; Chen, S. Eddy-mean flow interaction in the decadally modulating Kuroshio Extension system. *Deep Sea Res. II* **2010**, *57*, 1098–1110. [CrossRef]
42. Chiba, S.; Lorenzo, E.D.; Davis, A.; Keister, K.E.; Taguchi, B.; Sasai, Y.; Sugisaki, H. Large-scale climate control of zooplankton transport and biogeography in the Kuroshio-Oyashio Extension region. *Geophys. Res. Lett.* **2013**, *40*, 5182–5187. [CrossRef]
43. Lin, P.; Ma, J.; Chai, F.; Xiu, P.; Liu, H. Decadal variability of nutrients and biomass in the southern region of Kuroshio Extension. *Progr.Oceanogr.* **2020**, *188*, 102441. [CrossRef]
44. Hashioka, T.; Yamanaka, Y. Seasonal and regional variations of phytoplankton groups by top–down and bottom–up controls obtained by a 3D ecosystem model. *Ecol. Modell.* **2007**, *202*, 68–80. [CrossRef]
45. Zainuddin, M.; Saitoh, K.; Saitoh, S.I. Albacore (*Thunnus alalunga*) fishing ground in relation to oceanographic conditions in the western North Pacific Ocean using remotely sensed satellite data. *Fish. Oceanogr.* **2008**, *17*, 61–73. [CrossRef]
46. Yatsu, A.; Chiba, S.; Yamanaka, Y.; Ito, S.I.; Shimizu, Y.; Kaeriyama, M.; Watanabe, Y. Climate forcing and the Kuroshio/Oyashio ecosystem. *ICES J. Mar. Sci.* **2013**, *70*, 922–933. [CrossRef]
47. Niroumand-Jadidi, M.; Bovolo, F.; Bruzzone, L. Novel spectra-derived features for empirical retrieval of water quality parameters: Demonstrations for OLI, MSI, and OLCI Sensors. *IEEE T. Geosci. Remote.* **2019**, *57*, 10285–10300. [CrossRef]
48. Niroumand-Jadidi, M.; Bovolo, F.; Bruzzone, L. Water Quality Retrieval from PRISMA Hyperspectral Images: First Experience in a Turbid Lake and Comparison with Sentinel-2. *Remote Sens.* **2020**, *12*, 3984. [CrossRef]
49. Siegel, D.A.; Behrenfeld, M.J.; Maritorena, S.; McClain, C.R.; Antoine, D.; Bailey, S.W.; Bontempi, P.S.; Boss, E.S.; Dierssen, H.M.; Doney, S.C.; et al. Regional to global assessments of phytoplankton dynamics from the SeaWiFS mission. *Remote Sens. Environ.* **2013**, *135*, 77–91. [CrossRef]
50. Dee, D.P.; Uppala, S.M.; Simmons, A.J.; Berrisford, P.; Poli, P.; Kobayashi, S.; Andrae, U.; Balmaseda, M.A.; Balsamo, G.; Bauer, P.; et al. The ERA Interim reanalysis: Configuration and performance of the data assimilation system. *Q. J. R. Meteorol. Soc.* **2011**, *137*, 553–597. [CrossRef]
51. Locarnini, R.A.; Mishonov, A.V.; Baranova, O.K.; Boyer, T.P.; Zweng, M.M.; Garcia, H.E.; Reagan, J.R.; Seidov, D.; Weathers, K.; Paver, C.R.; et al. *World Ocean Atlas 2018, Temperature*; Mishonov, A., Ed.; NOAA Atlas NESDIS 81; NOAA: Silver Spring, MD, USA, 2018; Volume 1, 52p.
52. Garcia, H.E.; Boyer, T.P.; Baranova, O.K.; Locarnini, R.A.; Mishonov, A.V.; Grodsky, A.; Paver, C.R.; Weathers, K.W.; Smolyar, I.V.; Reagan, J.R.; et al. *World Ocean Atlas 2018: Product Documentation*; Mishonov, A., Ed.; NOAA: Ashville, NC, USA, 2019; Volume 1, 20p.
53. Kara, A.B.; Rochford, P.A.; Hurlburt, H.E. An optimal definition for ocean mixed layer depth. *J. Geophys. Res. Oceans* **2000**, *105*, 16803–16821. [CrossRef]
54. Hu, C.; Lee, Z.; Franz, B. Chlorophyll aalgorithms for oligotrophic oceans: A novel approach based on three-band reflectance difference. *J. Geophys. Res. Oceans* **2012**, *117*, C01011. [CrossRef]
55. Jing, Z.; Chang, P.; Shan, X.; Wang, S.; Wu, L.; Kurian, J. Mesoscale SST dynamics in the Kuroshio–Oyashio extension region. *J. Phys. Oceanogr.* **2019**, *49*, 1339–1352. [CrossRef]
56. Chelton, D.B.; Xie, S.P. Coupled ocean-atmosphere interaction at oceanic mesoscales. *Oceanography* **2010**, *23*, 52–69. [CrossRef]

57. Kuroda, H.; Takasuka, A.; Hirota, Y.; Kodama, T.; Ichikawa, T.; Takahashi, D.; Setou, T. Numerical experiments based on a coupled physical–biochemical ocean model to study the Kuroshio-induced nutrient supply on the shelf-slope region off the southwestern coast of Japan. *J. Mar. Syst.* **2018**, *179*, 38–54. [CrossRef]
58. Zhang, C.; Yao, X.; Chen, Y.; Chu, Q.; Yu, Y.; Shi, J.; Gao, H. Variations in the phytoplankton community due to dust additions in eutrophication, LNLC and HNLC oceanic zones. *Sci. Total Environ.* **2019**, *669*, 282–293. [CrossRef]
59. Obata, A.; Ishizaka, J.; Endoh, M. Global verification of critical depth theory for phytoplankton bloom with climatological in situ temperature and satellite ocean color data. *J. Geophys. Res. Oceans* **1996**, *101*, 20657–20667. [CrossRef]
60. Itoh, S.; Yasuda, I.; Saito, H.; Tsuda, A.; Komatsu, K. Mixed layer depth and chlorophyll a: Profiling float observations in the Kuroshio–Oyashio Extension region. *J. Mar. Syst.* **2015**, *151*, 1–14. [CrossRef]
61. Nakata, H.; Kimura, S.; Okazaki, Y.; Kasai, A. Implications of mesoscale eddies caused by frontal disturbances of the Kuroshio Current for anchovy recruitment. *ICES J. Mar. Sci.* **2000**, *57*, 143–152. [CrossRef]
62. Wang, Y. Composite of typhoon induced sea surface temperature and chlorophyll-a responses in the South China Sea. *J. Geophys. Res. Oceans* **2020**, *125*, e2020JC016243. [CrossRef]
63. Bakun, A.; Nelson, C.S. The seasonal cycle of wind-stress curl in subtropical eastern boundary current regions. *J. Phys. Oceanogr.* **1991**, *21*, 1815–1834. [CrossRef]
64. Chelton, D.B.; Davis, R.E. Monthly mean sea-level variability along the west coast of North America. *J. Phys. Oceanogr.* **1982**, *12*, 757–784. [CrossRef]
65. Chelton, D.B. Large-scale response of the California Current to forcing by wind stress curl. *CalCOFI Rep.* **1982**, *23*, 130–148.
66. Zhang, W.Z.; Wang, H.; Chai, F.; Qiu, G. Physical drivers of chlorophyll variability in the open South China Sea. *J. Geophys. Res. Oceans* **2016**, *121*, 7123–7140. [CrossRef]
67. Itoh, S.; Yasuda, I. Characteristics of mesoscale eddies in the Kuroshio–Oyashio Extension region detected from the distribution of the sea surface height anomaly. *J. Phys. Oceanogr.* **2010**, *40*, 1018–1034. [CrossRef]
68. Chelton, D.B.; Schlax, M.G.; Freilich, M.H.; Milliff, R.F. Satellite measurements reveal persistent small-scale features in ocean winds. *Science* **2004**, *303*, 978–983. [CrossRef]
69. Sato, N.; Nonaka, M.; Sasai, Y.; Sasaki, H.; Tanimoto, Y.; Shirooka, R. Contribution of sea-surface wind curl to the maintenance of the SST gradient along the upstream Kuroshio Extension in early summer. *J. Oceanogr.* **2016**, *72*, 697–705. [CrossRef]
70. Wang, Y.; Castelao, R.M. Variability in the coupling between sea surface temperature and wind stress in the global coastal ocean. *Cont. Shelf Res.* **2016**, *125*, 88–96. [CrossRef]
71. Jing, Z.; Wang, S.; Wu, L.; Chang, P.; Zhang, Q.; Sun, B.; Chen, Z. Maintenance of mid-latitude oceanic fronts by mesoscale eddies. *Sci. Adv.* **2020**, *6*, eaba7880. [CrossRef] [PubMed]
72. Ritchie, J.C.; Zimba, P.V.; Everitt, J.H. Remote sensing techniques to assess water quality. *Photogramm. Eng. Remote Sens.* **2003**, *69*, 695–704. [CrossRef]
73. Sugimoto, S.; Kobayashi, N.; Hanawa, K. Quasi-decadal variation in intensity of the western part of the winter subarctic SST front in the western North Pacific: The influence of Kuroshio Extension path state. *J. Phys. Oceanogr.* **2014**, *44*, 2753–2762. [CrossRef]
74. Chai, F.; Wang, Y.; Xing, X.; Yan, Y.; Xue, H.; Wells, M.; Boss, E. A limited effect of sub-tropical typhoons on phytoplankton dynamics. *Biogeosciences* **2021**, *18*, 849–859. [CrossRef]
75. Chai, F.; Johnson, K.S.; Claustre, H.; Xing, X.; Wang, Y.; Boss, E.; Riser, S.; Fennel, K.; Schofield, O.; Sutton, A. Monitoring ocean biogeochemistry with autonomous platforms. *Nat. Rev. Earth Environ.* **2020**, *1*, 315–326. [CrossRef]
76. Takahashi, T.; Sutherland, S.C.; Wanninkhof, R.; Sweeney, C.; Feely, R.A.; Chipman, D.W.; Hales, B.; Friederich, G.; Chavez, F.; Sabine, C.; et al. Climatological mean and decadal change in surface ocean pCO_2, and net sea–air CO_2 flux over the global oceans. *Deep Sea Res. II* **2009**, *56*, 554–577. [CrossRef]
77. NASA OBPG. *MODIS Aqua Global Level 3 Mapped SST. Ver. 2019.0*; PO.DAAC: Pasadena, CA, USA, 2020. [CrossRef]
78. Ocean Biology Processing Group, Ocean Ecology Laboratory, NASA Goddard Space Flight Center. *MODIS-Aqua Ocean Color Data*; Ocean Biology Processing Group, Ocean Ecology Laboratory, NASA Goddard Space Flight Center: Greenbelt, MD, USA, 2014. Available online: http://oceancolor.gsfc.nasa.gov/cgi/l3 (accessed on 16 December 2020).
79. Bechtold, P.; Köhler, M.; Jung, T.; Doblas-Reyes, F.; Leutbecher, M.; Rodwell, M.J.; Vitart, F.; Balsamo, G. Advances in simulating atmospheric variability with the ECMWF model: From synoptic to decadal time-scales. *Q. J. R. Meterol. Soc.* **2008**, *134*, 1337–1351. [CrossRef]
80. Thyng, K.M.; Greene, C.A.; Hetland, R.D.; Zimmerle, H.M.; DiMarco, S.F. True colors of oceanography: Guidelines for effective and accurate colormap selection. *Oceanography* **2016**, *29*, 9–13. [CrossRef]